Title

Macrophage centripetal migration drives spontaneous healing process after spinal cord injury

Journal

Science Advances, 5(5)

ISSN

2375-2548

Authors

Kobayakawa, Kazu
Ohkawa, Yasuyuki
Yoshizaki, Shingo
et al.

Publication Date

2019-05-03

DOI

10.1126/sciadv.aav5086

Peer reviewed

CELLULAR NEUROSCIENCE

Macrophage centripetal migration drives spontaneous healing process after spinal cord injury

Kazu Kobayakawa[1,2,3,4], Yasuyuki Ohkawa[5], Shingo Yoshizaki[1,2], Tetsuya Tamaru[1,2], Takeyuki Saito[2], Ken Kijima[1,2], Kazuya Yokota[2], Masamitsu Hara[2,3], Kensuke Kubota[2,4], Yoshihiro Matsumoto[2], Katsumi Harimaya[2], Keiko Ozato[6], Takahiro Masuda[7], Makoto Tsuda[8], Tomohiko Tamura[9], Kazuhide Inoue[7], V. Reggie Edgerton[3], Yukihide Iwamoto[10], Yasuharu Nakashima[2], Seiji Okada[1]*

Traumatic spinal cord injury (SCI) brings numerous inflammatory cells, including macrophages, from the circulating blood to lesions, but pathophysiological impact resulting from spatiotemporal dynamics of macrophages is unknown. Here, we show that macrophages centripetally migrate toward the lesion epicenter after infiltrating into the wide range of spinal cord, depending on the gradient of chemoattractant C5a. However, macrophages lacking interferon regulatory factor 8 (IRF8) cannot migrate toward the epicenter and remain widely scattered in the injured cord with profound axonal loss and little remyelination, resulting in a poor functional outcome after SCI. Time-lapse imaging and P2X/YRs blockade revealed that macrophage migration via IRF8 was caused by purinergic receptors involved in the C5a-directed migration. Conversely, pharmacological promotion of IRF8 activation facilitated macrophage centripetal movement, thereby improving the SCI recovery. Our findings reveal the importance of macrophage centripetal migration via IRF8, providing a novel therapeutic target for central nervous system injury.

INTRODUCTION

Spinal cord injury (SCI) is a devastating disorder resulting in permanent motor/sensory dysfunction (*1*). Mechanical injury causes bleeding and disruption of the blood–spinal cord barrier, followed by the infiltration of circulating cells such as macrophages and neutrophils (*2*). In the acute phase of SCI, these cells secrete tumor necrosis factor–α, interleukin-1β, and inducible nitric oxide synthase, inducing a secondary injury cascade that leads to demyelination and the loss of neuronal fibers around the originally injured site with deterioration of postinjury motor functional recovery (*1*, *3*–*6*). However, after the acute phase of SCI, little is known about the behavior of these cells.

In the post-acute phase, long-distance axonal retraction from the initial site of injury (called axonal dieback) occurs, and infiltrating macrophages touching axons exacerbate this axonal injury (*7*, *8*). However, in this phase, spontaneous tissue repair such as remyelination and axonal regeneration also occurs with partial motor recovery (*1*, *9*, *10*). To understand such complex pathophysiology, comprehensive screenings such as RNA sequencing (RNA-seq) can extract the factors involved in the recovery or progression of diseases (*11*–*13*).

In this study, we developed a time-course RNA-seq analysis protocol for SCI based on an established strategy (*14*), identifying a transcriptional factor, interferon regulatory factor 8 (IRF8), as a significantly increased factor during the recovery phase. We observed that infiltrating macrophages usually showed active migration to the injured site, but a lack of such macrophage migration in *IRF8*$^{-/-}$ mice had a negative impact on both damaged central nervous system (CNS) tissue and motor improvement after SCI. Furthermore, time-lapse imaging clarified the mechanism underlying macrophage migration via complement component C5a. Last, we showed that activating IRF8 contributed to macrophage migration and functional improvement, indicating a potential novel therapeutic intervention for SCI.

RESULTS

IRF8 expression is increased in the spinal cord after SCI

Although traumatic SCI results in residual motor/sensory paralysis, spontaneous functional recovery occurs to some extent after injury (*15*). In this study, we produced a contusion SCI (70 kilodynes) at the thoracic level of wild-type (WT) mice using a highly reproducible computer-controlled impactor and confirmed considerable recovery of the motor function for 2 weeks after SCI (*15*). To determine the genes that significantly increased expression levels in motor recovery phase, we performed a time-course genome-wide expression analysis. The heat map visually showed dynamic changes in expression of all genes at 4 to 14 days postinjury (dpi) (Fig. 1A). We initially expected that the genes involved in neural tissue regeneration or CNS repair would be enriched in the recovery phase of SCI. However, a gene ontology (GO) term analysis indicated that the genes involved in immune response, leukocyte activation, and chemotaxis were highly enriched, letting us further focus on the gene expression of leukocytes in the recovery phase of SCI (Fig. 1B). In the leukocyte-related genes, significant differences in the expression of *IRF8*, glycoprotein 49 A (*Gp49a*), and sulfatase 1 (*Sulf1*) were determined at 7 dpi by Cuffdiff (Fig. 1C) (*16*). Of these, the *IRF8* expression was consistently and significantly increased at 14 dpi (Fig. 1, D and E), which was further confirmed by a quantitative

[1]Department of Immunobiology and Neuroscience, Medical Institute of Bioregulation, Kyushu University, Fukuoka, Japan. [2]Department of Orthopedic Surgery, Graduate School of Medical Sciences, Kyushu University, Fukuoka, Japan. [3]Department of Integrative Biology and Physiology, University of California, Los Angeles, Los Angeles, CA, USA. [4]Department of Orthopedic Surgery, Spinal Injuries Center, Iizuka, Japan. [5]Division of Transcriptomics, Medical Institute of Bioregulation, Kyushu University, Fukuoka, Japan. [6]Program in Genomics of Differentiation, NICHD, National Institutes of Health, Bethesda, MD, USA. [7]Department of Molecular and System Pharmacology, Graduate School of Pharmaceutical Sciences, Kyushu University, Fukuoka, Japan. [8]Department of Life Innovation, Graduate School of Pharmaceutical Sciences, Kyushu University, Fukuoka, Japan. [9]Department of Immunology, Yokohama City University Graduate School of Medicine, Yokohama, Japan. [10]Kyushu Rosai Hospital, Kitakyushu, Japan.
*Corresponding author. Email: seokada@ortho.med.kyushu-u.ac.jp

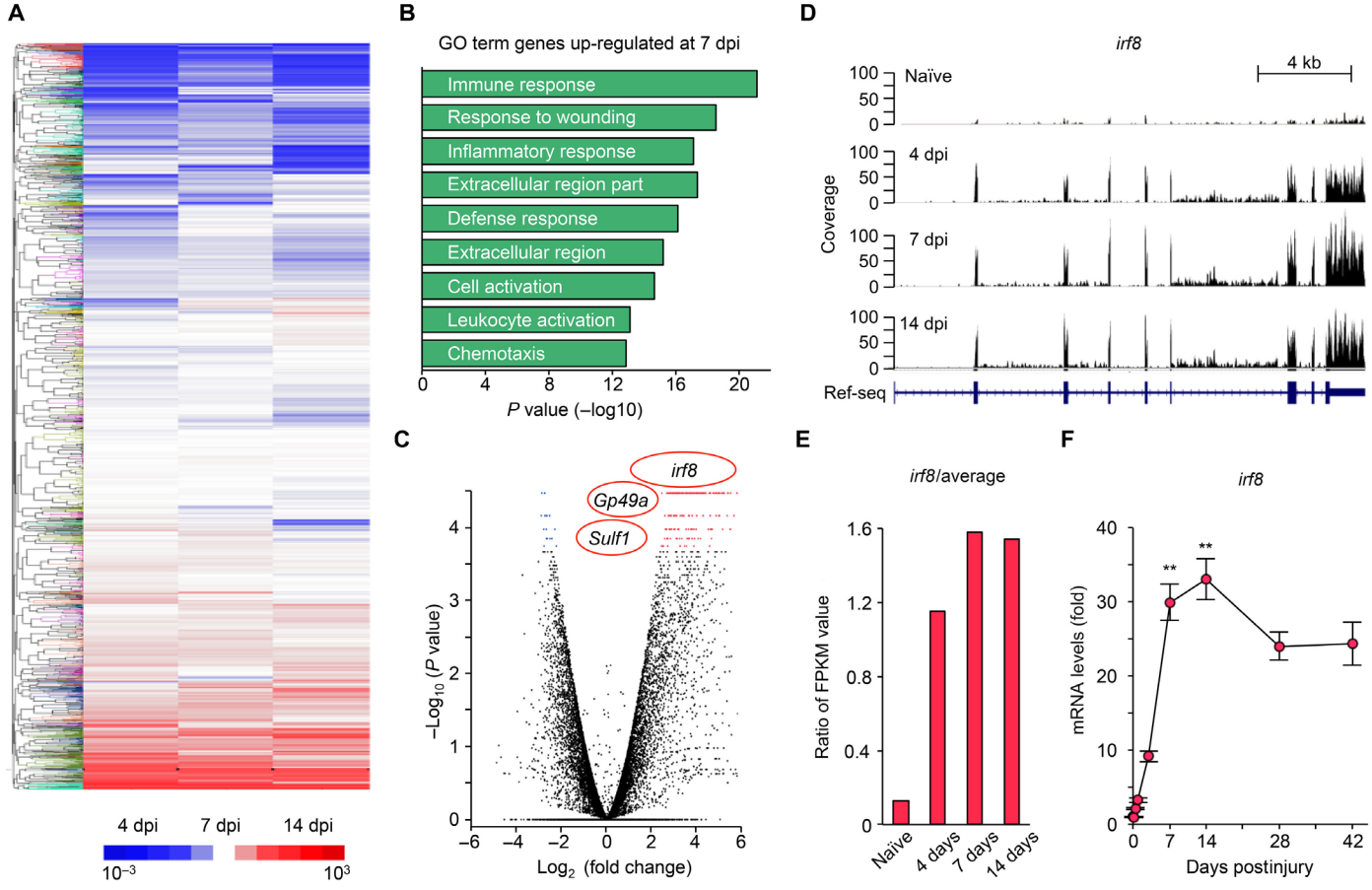

Fig. 1. A time-course RNA-seq analysis reveals prominent *IRF8* expression in the spinal cord during the recovery phase after SCI. (**A**) A heat map showing gene expression changes in the injured cord at 4, 7, and 14 dpi. Data from the samples of injured cords were normalized to those of uninjured cords. (**B**) GO term analysis of overexpressed (>10-fold change) genes in the RNA-seq analysis of the injured cord (7 dpi) compared to those of the uninjured cord. Lists show the top nine GO terms obtained ranked by *P* value (Fisher's exact test with Benjamini-Hochberg correction). (**C**) Volcano plot of the gene expression differences between the injured cord (7 dpi) and uninjured cord. Red or blue dots indicate significantly up-regulated or down-regulated genes, respectively. (**D**) Wiggle plots showing the coverage of each exon for *IRF8* before injury and at 4, 7, and 14 dpi. Ref-seq, reference sequencing. (**E**) Ratio of the fragments per kilobase of exon per million mapped sequence reads (FPKM) value of *IRF8* to the mean FPKM value of all expressed genes at each time point after SCI. (**F**) Significantly increased mRNA expression of *IRF8* analyzed with qPCR in spinal cords before and after injury ($n = 5$ per each time point). The data shown in (A) to (E) are representative of four samples per time point. $^*P < 0.05$ and $^{**}P < 0.001$, one-way analysis of variance (ANOVA) with Dunnett's test for multiple comparisons against the uninjured control group (F). The data are presented as the means ± SEM.

polymerase chain reaction (qPCR) analysis (Fig. 1F). We therefore focused on the IRF8 function during SCI recovery.

IRF8 is selectively expressed in CD68$^+$ cells after SCI

Macrophages [CD68$^+$ in injured spinal cord (*6*)] express IRF8. To identify IRF8 localization, we performed an immunohistochemical analysis of the injured spinal cord. Whereas no IRF8 expression was detected in polymorphonuclear (PMN)–positive neutrophils, CD3$^+$ T cells, glial fibrillary acidic protein (GFAP)–positive astrocytes, neuronal nuclei (NeuN)–positive neurons, or glutathione *S*-transferase (GST)–π–positive oligodendrocytes, all IRF8$^+$ cells were CD68$^+$ in the injured cord (Fig. 2, A to H). These results were confirmed by a PCR analysis with selectively isolated mRNA from these cells using flow cytometry or laser microdissection (LMD) (Fig. 2I). Notably, at 4 dpi, IRF8 was located in the cytoplasm and nucleus of CD68$^+$ cells but localized in the nucleus at 7 dpi, suggesting that IRF8 nuclear translocation and its transcriptional activity were enhanced at 7 dpi (Fig. 2, B and C).

IRF8 is crucial for the epicenter-directed macrophage migration in the injured spinal cord

To investigate the role of IRF8 in macrophage behavior after SCI, we first performed quantitative analysis of infiltrating macrophages in WT and *IRF8*$^{-/-}$ mice using the cell sorter (*15*, *17*). As previously described, CD45$^+$ cells obtained from the spinal cord tissue were subdivided into three populations on the basis of expression of the surface markers, and the CD11b^{high}/Ly6G^{nega}/CD45^{high} population was isolated as infiltrating macrophages (*4*, *15*). The quantitative analysis and gene expression analysis demonstrated that IRF8 did not affect the cell number and polarization of infiltrating macrophages after SCI (Fig. 3, A and B, and fig. S1) (*3*, *6*, *18*). Next, we performed immunohistochemical analysis of injured spinal cords of these mice and observed that the location of CD68$^+$ cells in the injured cord of WT mice gradually shifted toward the lesion epicenter from 4 to 42 dpi (Fig. 3, C and D). However, we found that the CD68$^+$ cells of *IRF8*$^{-/-}$ mice remained widely scattered over the injured cord

until 42 dpi (Fig. 3, C and D). A histological quantitative analysis confirmed that the craniocaudal ranges of CD68$^+$ cells of *IRF8*$^{-/-}$ mice were significantly broader than those of WT mice at 7, 14, and 42 dpi, respectively (Fig. 3E). These results suggested that the infiltrating WT macrophages migrated toward the epicenter, while the *IRF8*$^{-/-}$ macrophages did not.

Peripheral blood–derived macrophages migrate toward epicenter after SCI via IRF8

Because both peripheral blood–derived macrophages and spinal cord–resident microglia are CD68$^+$/IRF8$^+$ and immunohistologically indistinct from one another (*4*, *8*, *19*), the IRF8-dependent migration of CD68$^+$ cells might be due to resident microglia. To investigate this issue, we developed two bone marrow chimeric mice models: microglial IRF8–deficient and macrophagic IRF8–deficient chimeric mice, as previously described (fig. S2A) (*20*). These chimeric mice revealed that IRF8-dependent migration of CD68$^+$ cells is due to microphages, not to microglia, and that microglial IRF8 had no significant influence on functional outcomes after SCI (fig. S2, B to F). Therefore, we further explored the influence of IRF8 in peripheral blood–derived macrophages on the pathophysiology after SCI.

To directly test the migration ability of WT and *IRF8*$^{-/-}$ macrophages in vivo, we performed one-shot injection of *IRF8*$^{+/+}$-enhanced green fluorescent protein–positive (EGFP$^+$) or *IRF8*$^{-/-}$-EGFP$^+$ CD11b^{posi}/Ly6G^{nega}/CD115^{posi} peripheral blood–derived monocytes, which differentiate to macrophages in injured spinal cords (*21*), into 2 mm rostral to the epicenter of the WT spinal cord immediately after SCI (fig. S3). Analyzing the time-course sections of these injured cords, we found that the injected EGFP$^+$-*IRF8*$^{+/+}$ CD68$^+$ cells migrated toward the epicenter of the injured cord (Fig. 3, F and G). In contrast, the injected EGFP$^+$-*IRF8*$^{-/-}$ CD68$^+$ cells remained at the site of injection until 14 dpi (Fig. 3, F and G). These results indicated that WT macrophages actually migrate toward the epicenter, while migration of *IRF8*$^{-/-}$ macrophages is critically impaired. However, there remained a possibility that some WT macrophages far from the epicenter might have disappeared, with other macrophages newly infiltrating near the epicenter. To clarify this issue, we performed daily intravenous injection of EGFP$^+$ monocytes after SCI (Fig. 3H). When *IRF8*$^{+/+}$-EGFP$^+$ or *IRF8*$^{-/-}$-EGFP$^+$ monocytes were intravenously injected from 1 to 3 dpi, they infiltrated to spinal cords; however, the monocytes injected intravenously after 4 dpi did not infiltrate in the injured cord from the peripheral blood (Fig. 3I and fig. S4). Together with the result of spinal injection of monocytes, we found that the translocation of macrophages in the injured spinal cord was not due to later infiltration into the central region but due to the actual migration toward the epicenter via IRF8.

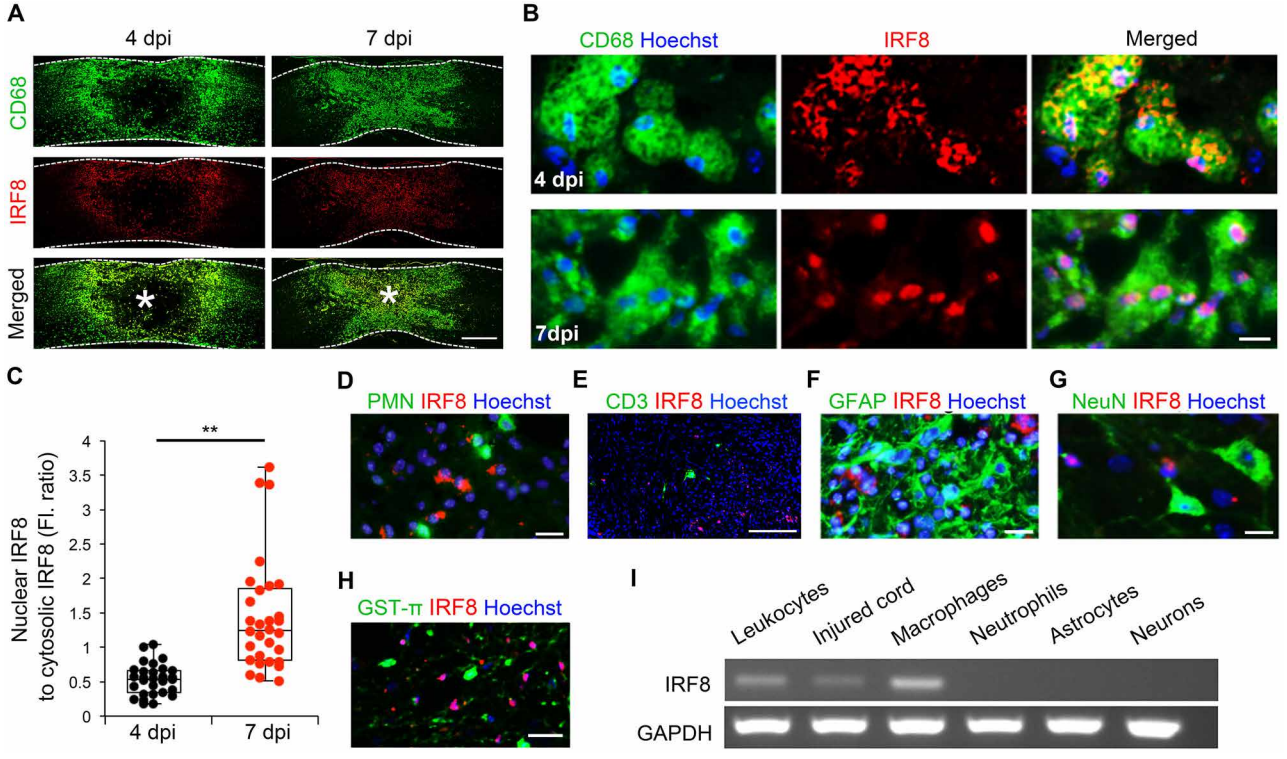

Fig. 2. IRF8 is expressed in CD68$^+$macrophages after SCI. (**A**) Representative images of immunofluorescent staining of spinal cord with CD68 (green) and IRF8 (red) in WT mice at 4 and 7 dpi. The asterisks indicate the lesion epicenter. (**B**) CD68 (green) and IRF8 (red) double-positive macrophages in the perilesional areas. The nuclei were counterstained with Hoechst 33258 dye (blue). Selective localization of IRF8 in the nuclei of macrophages was observed at 7 dpi (bottom). All IRF8-expressing cells were CD68$^+$. (**C**) Fluorescence ratio (Fl. ratio) of nuclear IRF8 to cytosolic IRF8 (n = 30 cells per group). (**D** to **H**) Double immunostaining of IRF8 with PMN, CD3, GFAP, NeuN, and GST-π. (**I**) The IRF8 expression examined by reverse transcription PCR (RT-PCR) in selectively isolated macrophages, neutrophils, reactive astrocytes, and neurons. Among these cells, the IRF8 expression was observed only in macrophages. The data shown in (I) are representative of three samples from three mice/each cell fraction. Images shown in (A), (B), and (D) to (H) are representative of eight sections per four mice. The images were obtained from two independent experiments. Scale bars, 500 μm (A), 20 μm (E and G), and 10 μm (B, D, F, and H). **P < 0.005, Wilcoxon rank-sum test. The data are presented as means ± SEM. GAPDH, glyceraldehyde-3-phosphate dehydrogenase.

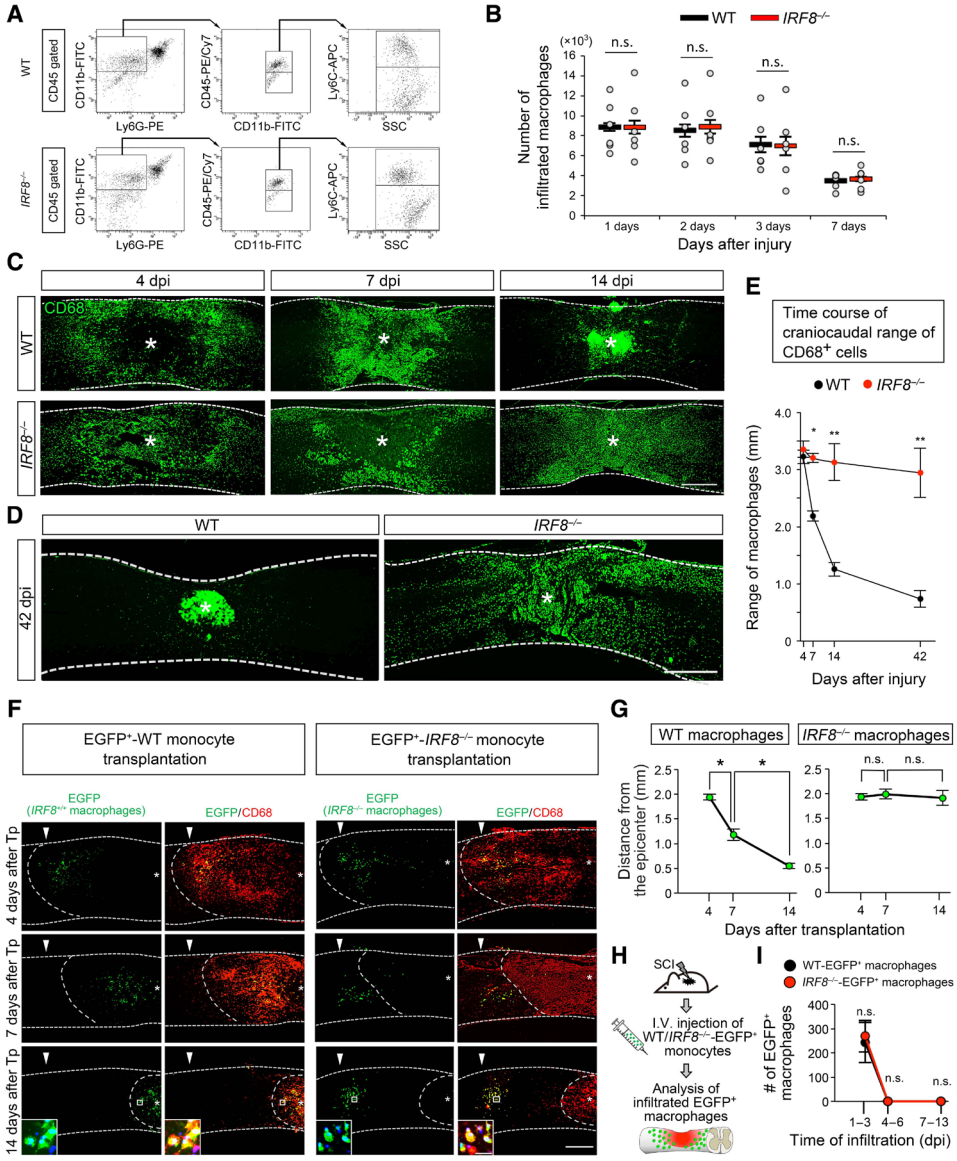

Fig. 3. IRF8 is required for macrophage migration toward the epicenter in the injured spinal cord during the recovery phase. (**A**) CD45-gated cells in the injured cord were divided into CD11b^{+}/CD45^{high}/Ly6G^{-} infiltrating macrophages. The cell numbers of these macrophages in the injured cord of WT/*IRF8*$^{-/-}$ mice were quantitatively counted using the FACS software program. FITC, fluorescein isothiocyanate; PE, phycoerythrin; SSC, side scatter; APC, allophycocyanin. (**B**) The cell numbers of macrophages in the injured cord of *IRF8*$^{-/-}$ mice were comparable to those of WT mice after SCI ($n = 6$ per group). Although *IRF8*$^{-/-}$ mice generate reduced numbers of monocytes/macrophages (*66*), these results indicate that macrophage infiltration into the injured spinal cord does not require IRF8. n.s., not significant. (**C**) Change in the distribution of CD68^{+} macrophages over time. The location of macrophages shifted toward the lesion epicenter from 4 to 14 dpi after injury in WT mice, whereas the macrophages of *IRF8*$^{-/-}$ mice remained widely scattered in the injured cord. The fine lines indicate the outlines of the spinal cords. Asterisk indicates the epicenter of the lesion. (**D**) Distribution of macrophages in WT or *IRF8*$^{-/-}$ mice at 42 dpi. The fine lines indicate the outlines of the spinal cords. Asterisk indicates the epicenter of the lesion. (**E**) Comparison of the craniocaudal distribution of macrophages in injured cords between WT and *IRF8*$^{-/-}$ mice ($n = 8$ WT, 7 *IRF8*$^{-/-}$ mice per group at each time point, respectively). (**F**) EGFP^{+}-*IRF8*$^{+/+}$ (left) or EGFP^{+}-*IRF8*$^{-/-}$ (right) monocytes isolated from the peripheral blood of EGFP^{+}-*IRF8*$^{+/+}$ or EGFP^{+}-*IRF8*$^{-/-}$ mice as EGFP^{posi}/CD11b^{posi}/Ly6G^{nega}/CD115^{posi} monocytic population (fig. S3), respectively, were injected into 2 mm rostral to the epicenter of the injured spinal cord of WT mice once immediately after SCI. Representative images of the immunofluorescent staining of spinal cord injected with these monocytes after SCI. Tp; transplantation of EGFP^{+} monocytes. The fine broken lines indicate the outlines of the spinal cords. The coarse broken lines indicate the area of the EGFP^{-}/CD68^{+} host macrophages. The asterisks indicate the epicenters of injured spinal cord. The arrowheads indicate the injection point of the EGFP^{+} macrophages. Inset: High-magnification image. The nucleus was counterstained with Hoechst 33258 dye (blue). Scale bar, 20 μm. The images shown are representative of six slides from three mice per time point per group. (**G**) Distances of EGFP^{+}-*IRF8*$^{+/+}$ or EGFP^{+}-*IRF8*$^{-/-}$ macrophages from the epicenter at each time point ($n = 6$ sections/three mice per each time point per group). (**H**) Schematic representation of intravenous (I.V.) injection of EGFP^{+}-*IRF8*$^{+/+}$ or EGFP^{+}-*IRF8*$^{-/-}$ monocytes after SCI. EGFP^{+}-*IRF8*$^{+/+}$ or EGFP^{+}-*IRF8*$^{-/-}$ monocytes were daily injected intravenously from 1 to 3, 4 to 6, or 7 to 13 dpi. (**I**) Quantitative analysis of the infiltrating EGFP^{+} macrophages in the injured cord of mice intravenously injected with EGFP^{+} macrophages from 1 to 3, 4 to 6, or 7 to 13 dpi ($n = 4$ sections/four mice per group) (see also fig. S4). The images shown in (C) and (D) are representative of eight or seven slides from eight WT/seven *IRF8*$^{-/-}$ mice per each time point. Scale bars, 500 μm (C, D, and F). *$P < 0.05$ and **$P < 0.005$, Wilcoxon rank-sum test (B), two-way repeated-measures ANOVA with the Tukey-Kramer post hoc test (E and I), and ANOVA with the Tukey-Kramer post hoc test (G). The data are presented as means ± SEM (B, E, G, and I).

The widely scattered *IRF8*$^{-/-}$ macrophages caused the profound neural damage and the poor functional recovery after SCI

Given that infiltrating macrophages in touch with axons directly exacerbate axonal dieback (*8*), we next investigated the 5-hydroxytryptamine (5HT)–positive axons in *IRF8*$^{-/-}$ mice after SCI and found that *IRF8*$^{-/-}$ mice had significantly fewer 5HT^{+} axons than WT mice at 42 dpi (Fig. 4, A and B, and fig. S5, A to E), suggesting that a wide range of scattered *IRF8*$^{-/-}$ macrophages may be involved in this profound axonal loss. Because the spared axons are needed for remyelination after SCI (*22*), Luxol fast blue (LFB) staining (myelin sheath staining) was performed. Accompanied with the few 5HT^{+} axons and widely scattered macrophages, *IRF8*$^{-/-}$ mice showed a significantly decreased LFB^{+} area compared with WT mice at 42 dpi, although the LFB^{+} area in *IRF8*$^{-/-}$ mice was comparable to that in WT mice both before injury and at 7 dpi, respectively, indicating remyelination disorder after SCI in *IRF8*$^{-/-}$ mice (Fig. 4, C to E, and fig. S5, F to I). The myelin sheath area had a strong, negative correlation with the area of CD68^{+} cells, supporting the role of widely scattered *IRF8*$^{-/-}$ macrophages in axonal loss and subsequent remyelination disorder (Fig. 4F). In addition, migration of astrocytes and astroglial formation were impaired, and neuronal loss was exacerbated in *IRF8*$^{-/-}$ mice compared with WT mice after SCI (fig. S5, J to Q). The area of demyelination, astrocytes migration, glial scar formation, and neuronal loss after SCI are associated with decrease in functional recovery (*4*, *9*, *23*). Here, *IRF8*$^{-/-}$ mice exhibited worse functional outcomes after SCI compared with WT mice, as measured by the Basso Mouse Scale (BMS) score, foot print analysis, and grip walk test (Fig. 4, G to J) (*24*, *25*).

To investigate the possibility that *IRF8*$^{-/-}$ macrophages might modulate the plasticity after SCI through cytokine expression, we performed RNA-seq analysis of both WT and *IRF8*$^{-/-}$ mice. Pathway analysis detected significantly enriched KEGG (Kyoto Encyclopedia of Genes and Genomes) pathways related to cytokines after SCI in WT mouse, but the RNA-seq analysis and gene expression analysis in macrophages showed comparable expression levels of these cytokines between WT and *IRF8*$^{-/-}$ genotypes, indicating that IRF8 did not determine cytokine expression levels in macrophages or spinal cords (figs. S6 to S15) (*3*, *26*). These findings indicated that *IRF8*$^{-/-}$ macrophages caused the poor histopathological outcomes leading to the worse functional recovery due to impaired migration toward the epicenter after SCI.

IRF8 influences the migration capability of macrophages in the gradient of complement component C5a

We next explored what factors attract the macrophages centripetally. To date, complement component C5a, fractalkine, and Reg3β have been reported as chemoattractants for macrophages (*12*, *27*, *28*). An immunohistochemical analysis revealed a strong C5a expression in the epicenter (Fig. 5A). Therefore, we further analyzed the C5a gradient and found that the C5a expression gradually increased when approaching the epicenter, suggesting that C5a at the epicenter attracted the macrophages (Fig. 5B). To verify the role of C5a on macrophage migration, C5a was ectopically injected rostral and caudal to the epicenter from 4 to 7 dpi. The macrophages migrated toward both C5a injection sites and the epicenter and were widely scattered, directly indicating that epicenter-directed macrophage migration was dependent on the C5a concentration (Fig. 5, C and D). Accompanied with widely scattered macrophages, the number of NeuN^{+} neurons in the mice with C5a injection after SCI was significantly reduced compared with that with phosphate-buffered saline (PBS) injection (fig. S16, A to C). In addition, functional recovery was deteriorated by the C5a injection (fig. S16D). These results indicated the detrimental effect of the impaired migration of infiltrating macrophages after SCI. To investigate the *IRF8*$^{-/-}$ macrophage migration with C5a, time-lapse phase-contrast imaging was performed. In the stable C5a gradient, WT macrophages rapidly migrated toward higher C5a concentrations with a strong directionality, represented by the chemotaxis index (Fig. 5, E to H, and movie S1). However, *IRF8*$^{-/-}$ macrophages showed extraordinarily low displacement and decreased directionality to C5a (Fig. 5, E to H, and movie S2). These results indicated that the *IRF8*$^{-/-}$ macrophages failed to migrate toward the epicenter in the injured cord due to impaired directional movement toward C5a at the epicenter. To approach the mechanisms behind the C5a-directed macrophage migration via IRF8 signaling, we first investigated receptors of C5a, but the expression levels of *C5ar1* and *C5ar2* (coding the receptors of C5a) were comparable between WT and *IRF8*$^{-/-}$ macrophages (fig. S17) (*29*, *30*). Next, we analyzed the purinergic receptor pathway because macrophages release adenosine triphosphate (ATP) in C5a gradient in a paracrine manner, and ATP and its degradation products (adenosine diphosphate and adenosine) bind to the purinergic receptors to drive macrophage migration by inducing lamellipodial membrane protrusions (*28*). *IRF8*$^{-/-}$ macrophages exhibited significantly lower expression levels of purinergic receptors than *IRF8*$^{+/+}$ macrophages (Fig. 5I), suggesting IRF8 control macrophage migration via purinergic receptors expression. To further investigate whether purinergic receptors have a significant role in macrophagic migration after SCI, we blocked purinergic receptor signaling using inhibitors after SCI. Following the previous study demonstrating that triple and cocktail block of purinergic receptors could inhibit macrophagic migration (*28*), we injected AR-C69931MX (P2Y12R inhibitor), AR-C118925XX (P2Y2R inhibitor), 8-SPT (A2a-A3 inhibitor), MRS-2179 (P2Y1R inhibitor), and NF-449 (P2X1R and P2X4R inhibitor) into spinal cord of WT mice from 4 to 12 dpi. The injection with AR-C69931MX, AR-C118925XX and 8-SPT (triple block) inhibited migration of macrophages after SCI (Fig. 5, J and K). Moreover, we found that the migration failure of macrophages with AR-C69931MX, AR-C118925XX, 8-SPT, MRS-2179, and NF-449 (cocktail block) was severer than that with triple block (Fig. 5, J and K). These results indicate that IRF8 regulates the expression of purinergic receptors that is important for macrophagic centripetal migration after SCI.

Activation of IRF8 signaling enhanced epicenter-directed migration of macrophages and functional recovery after SCI

IRF8 was activated and translocated into nuclei of macrophages at 7 dpi with epicenter-directed migration (Figs. 2 and 3). To further investigate whether the activation of IRF8 promotes macrophage migration, EGFP^{+} macrophages with IRF8 activation were isolated from the injured cords of chimeric mice with EGFP^{+} *IRF8*$^{+/+}$ macrophages and EGFP^{-} *IRF8*$^{+/+}$ microglia at 7 dpi, and EGFP^{+} macrophages without IRF8 activation were isolated from the chimeric mice at 4 dpi; we then transplanted them into WT spinal cords immediately after SCI and observed that macrophages with IRF8 activation migrated faster than those without IRF8 activation and were more tightly compacted than the host macrophages at 7 days after transplantation (Fig. 6, A to C, and fig. S18). These results indicated that

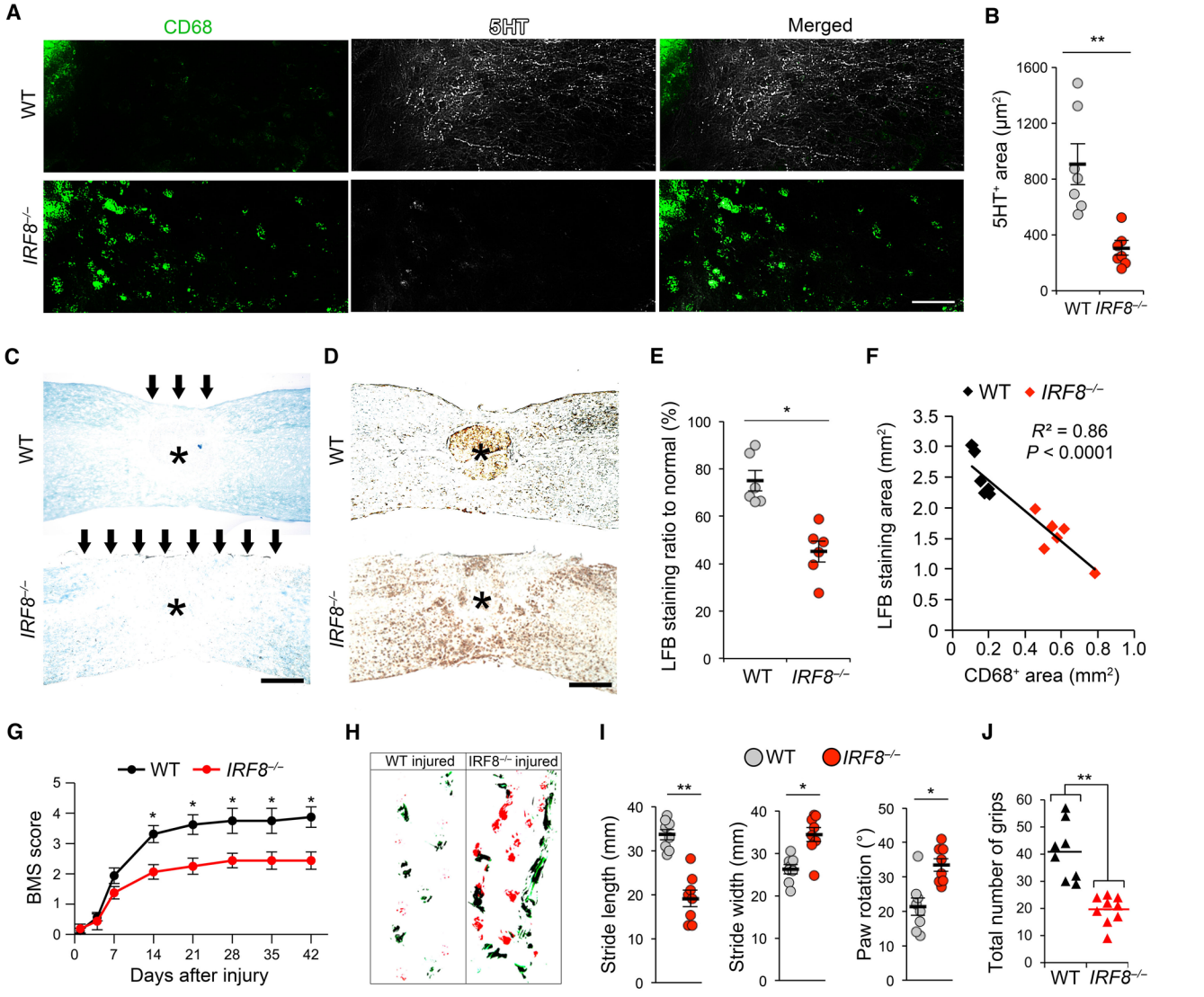

Fig. 4. Widely scattered macrophages in *IRF8*$^{-/-}$ mice caused the widespread lesion and the poor functional recovery after SCI. (**A**) 5HT (white) and CD68 (green) staining of the injured cords of WT and *IRF8*$^{-/-}$ mice at 42 dpi (representative images of seven sections from seven mice per group). (**B**) Quantification of the 5HT^{+} area per 4.0×10^5 μm^2 at 42 dpi ($n = 7$ sections/seven mice per group). (**C**) LFB staining showed a greater demyelinated lesion (arrows) area in *IRF8*$^{-/-}$ mice than in WT mice at 42 dpi. The asterisk indicates the lesion epicenter. (**D**) Immunohistochemical staining showed CD68^{+} macrophages located in the LFB-negative demyelinated area of the serial section shown in (C). The asterisk indicates the lesion epicenter. (**E**) Quantification of the area of LFB^{+} myelin at 42 dpi ($n = 6$ per group). (**F**) A linear regression analysis showing the negative correlation between the CD68^{+} and LFB^{+} areas at 42 dpi (β = −2.49; 95% confidence interval, −3.19 to −1.79). (**G**) Time course of the functional recovery of the BMS score after SCI ($n = 8$ per group). (**H**) A footprint analysis performed at 42 dpi showed that *IRF8*$^{-/-}$ mice were unable to consistently step. (**I**) Quantification of the footprint analysis after SCI showing significantly worse motor functions in *IRF8*$^{-/-}$ mice than in WT mice at 42 dpi ($n = 8$ per group). (**J**) Scores for the grip walk test in each mouse at 42 dpi. The images shown in (C) and (D) are representative of six slides from six mice per each group. Scale bars, 50 μm (A) and 500 μm (C and D). *$P < 0.05$ and **$P < 0.005$, Wilcoxon rank-sum test (B, E, I, and J) and two-way repeated-measures ANOVA with the Tukey-Kramer post hoc test (G). The data are presented as means ± SEM (B, E, G, and I).

IRF8 activation accelerated epicenter-directed macrophage migration.

These findings led us to explore whether enhancing IRF8 activation could improve the SCI recovery. To test this, we administered a combination of interferon-γ (IFN-γ) and lipopolysaccharide (LPS), which strongly activates IRF8 (*31*). Before this in vivo experiment, we evaluated the efficacy of the combination in vitro. Without the combination, most of the IRF8 was located in the cytoplasm; however, immediately after stimulation, IRF8 nuclear translocation was observed accompanied by significantly increased gene expression of purinergic receptors (Fig. 6, D to F). For the in vivo combination administration, spinal injections were performed after 48 hours post-injury (hpi) (Fig. 6G) to avoid possible exacerbation of acute inflammatory reaction after SCI, which peaked between 3 and 12 hours hpi and thereafter resolved by 24 hpi, as reported previously (*24*, *32*). Actually, we did not observe any harmful effects of this combination injection such as systemic inflammation and neuropathic pain after SCI (*19*, *33*), supporting the feasibility of this therapy (fig. S19,

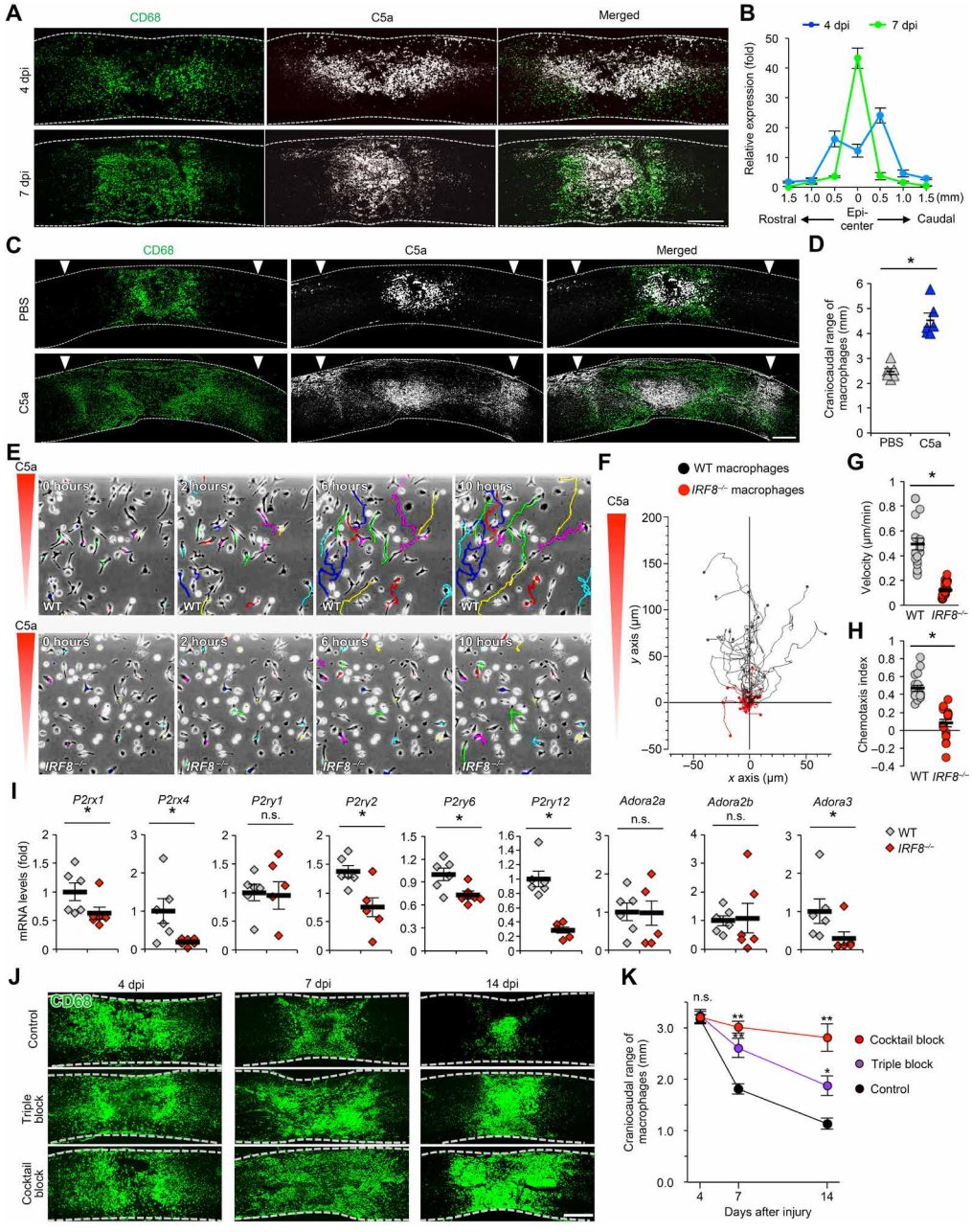

Fig. 5. Macrophages migrate to high concentrations of complement component C5a at the lesion epicenter via purinergic receptors. (**A**) Representative images of the immunohistochemical analysis of the spatiotemporal distribution of CD68 (green) and C5a (white) in the injured cord after SCI. The $C5a^+$ area was located medially in the $CD68^+$ area. (**B**) The C5a expression patterns were dependent on the distance from the lesion epicenters. The C5a expression gradient was observed at 4 and 7 dpi, and the expression of C5a peaked at the lesion epicenter at 7 dpi ($n = 8$ samples from eight mice/each group/each time point). (**C**) Representative images of the immunohistochemical analysis of the injured spinal cord obtained from WT mice daily injected with C5a rostral and caudal to the lesion epicenter from 4 to 7 dpi. $CD68^+$ macrophages were attracted to the C5a injection sites. The arrowheads indicate the injection sites of PBS or C5a. (**D**) A comparison of the craniocaudal distribution of macrophages between the C5a- and PBS-injected spinal cord at 7 dpi ($n = 8$ samples from eight mice per group). (**E**) Time-lapse phase-contrast microscopy image sequences of macrophages in the C5a gradient. WT macrophages migrated toward higher concentrations of C5a, whereas $IRF8^{-/-}$ macrophages did not migrate when exposed to a C5a chemotactic gradient. (**F**) Migration plots of WT (black dots and lines) and $IRF8^{-/-}$ (red dots and lines) macrophages in a gradient of C5a. The starting point of each track was normalized to the position $x = 0$ and $y = 0$. The positive values on the y axis represent movement in the direction of the source of C5a ($n = 18$ per group). (**G**) Mean velocities of WT and $IRF8^{-/-}$ macrophages treated with C5a ($n = 18$ per group). (**H**) Mean chemotaxis indices of WT and $IRF8^{-/-}$ macrophages treated with C5a ($n = 18$ per group). (**I**) mRNA expression in the isolated WT and $IRF8^{-/-}$ macrophages ($n = 6$ samples per group). (**J**) Representative images of the immunohistochemical analysis of the CD68 macrophages after blockade of purinergic signaling in the injured cord. Inhibitors of purinergic receptors or PBS were injected every other day from 4 dpi. (**K**) Quantitative analysis of craniocaudal range of $CD68^+$ macrophages with PBS injection (control), triple block, or cocktail block ($n = 10$ samples from 10 mice per group). The images shown in (A) and (C) are representative of eight slides from eight mice per group or time point. Scale bars, 500 μm. $^*P < 0.05$ and $^{**}P < 0.005$, Wilcoxon rank-sum test (D, G, H, and I) and two-way repeated-measures ANOVA with the Tukey-Kramer post hoc test (K). The data are presented as means ± SEM.

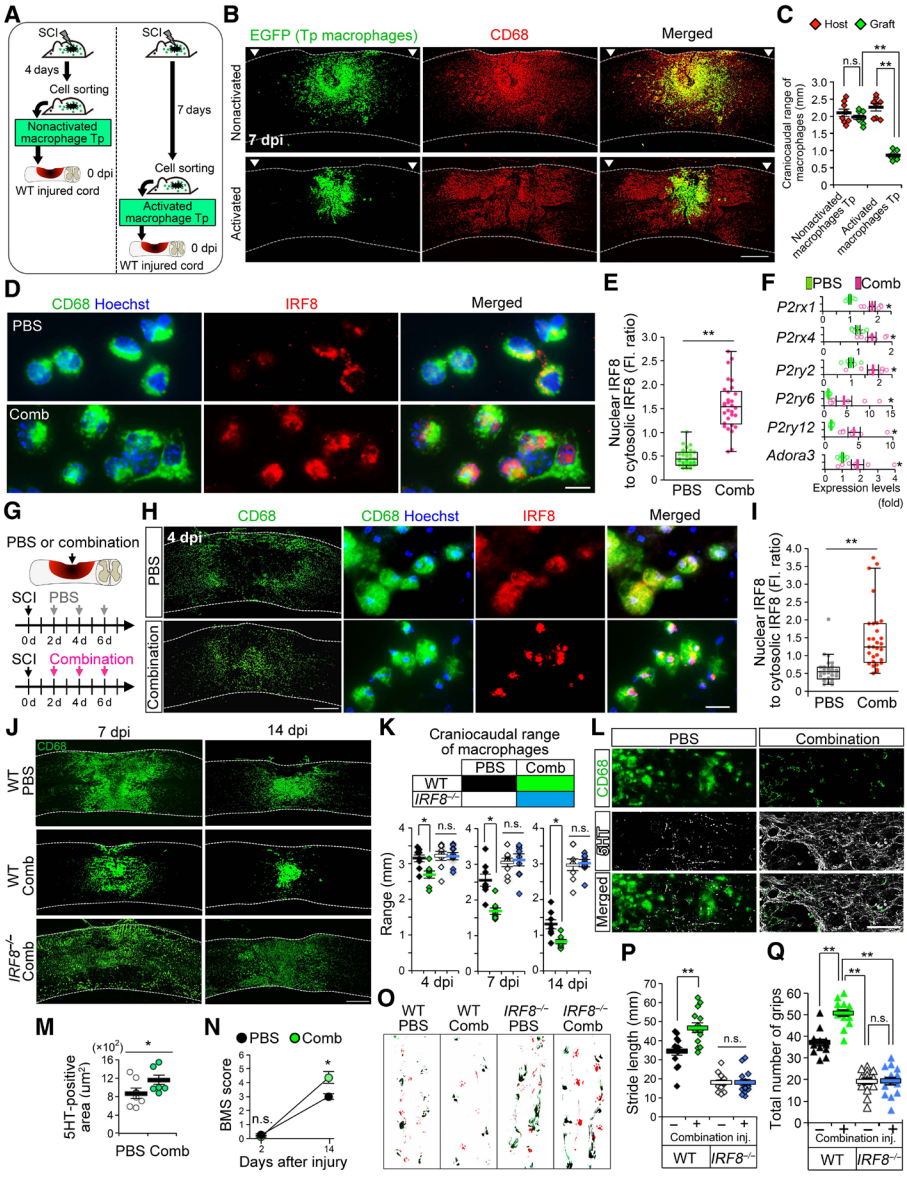

Fig. 6. Activating IRF8 promotes macrophage migration during the recovery phase after SCI. (**A**) Macrophage transplantation protocol. Using a cell sorter, IRF8-activated and nonactivated macrophages were isolated from injured cords at 4 and 7 dpi of EGFP$^+$ bone marrow chimeric mice, respectively. These cells were transplanted into the spinal cord of EGFP$^-$ WT mice immediately after SCI. (**B**) Representative images of the immunohistochemical analysis of injured spinal cords transplanted with IRF8-activated or nonactivated macrophages. The arrowheads indicate the injection sites of macrophages. (**C**) Craniocaudal distribution of the transplanted IRF8-activated macrophages compared with the transplanted nonactivated macrophages in the injected spinal cord at 7 dpi ($n = 8$ sections/four mice per group). (**D**) Immunocytochemical analysis of the IRF8 translocation into the nuclei of macrophages differentiated from isolated CD11b$^+$/CD45^{high}/Ly6G$^-$ peripheral blood–derived monocytes 3 hours after IFN-γ and LPS combination stimulation, stained with CD68 (green), IRF8 (red), and Hoechst (blue). (**E**) Fluorescence ratio of nuclear IRF8 to cytosolic IRF8 ($n = 30$ cells per group). (**F**) mRNA expression of purinergic receptors in macrophages 3 hours after combination stimulation ($n = 8$ dishes per group). (**G**) Schedule of in vivo combination injection after SCI. PBS or combination was injected into the spinal cord after SCI. (**H**) Representative images of the immunohistochemical analysis of the injured cord receiving the combination injection. CD68$^+$ macrophages with combination injection rapidly migrated toward the lesion epicenter at 4 dpi. Increased nuclear translocation of IRF8 of macrophages was shown in the injured cord with combination injection. Scale bars, 500 μm (left) and 10 μm (right). (**I**) Ratio of nuclear IRF8 to cytosolic IRF8 of macrophages in the injured cord with PBS or combination injection at 4 dpi ($n = 30$ cells from eight slides per eight mice per group). (**J**) Time course of macrophage migration in the injured cord with the combination injection. (**K**) Comparison of the craniocaudal distribution of WT/*IRF8*$^{-/-}$ macrophages with combination injection and those with PBS injection ($n = 8$ per group per time point). (**L**) Representative images of the immunofluorescent staining of spinal cord with PBS/combination injection at 14 dpi. (**M**) Quantification of the 5HT$^+$ area of spinal cord with PBS/combination injection at 14 dpi (eight sections/eight mice per group). (**N**) BMS score of WT mice with PBS or combination injection ($n = 8$ mice per group). (**O**) Footprint analysis of WT/*IRF8*$^{-/-}$ mice with combination injection compared to those with PBS injection at 14 dpi. (**P**) Stride length of WT/*IRF8*$^{-/-}$ mice with PBS and combination injection at 14 dpi ($n = 14$ mice per group). (**Q**) Scores of the grip walk test in each mouse at 14 dpi ($n = 14$ per group). Scale bars, 500 μm (B and J), 10 μm (D), and 100 μm (L). The images shown in (H), (J), and (L) are representative of eight slides from eight mice/each group per time point. *$P < 0.05$ and **$P < 0.005$, Wilcoxon rank-sum test (E, F, I, and M), ANOVA with the Tukey-Kramer post hoc test (C, K, P, and Q) and two-way repeated-measures ANOVA with the Tukey-Kramer post hoc test (N). The data are presented as means ± SEM. (C, F, K, M, N, P, and Q).

A and B). The combination injection successfully activated macrophagic IRF8 with enhanced nuclear translocation (Fig. 6, H and I). The mice with the combination injection showed greater promotion of macrophage migration than those with PBS injection, accompanied by a significantly large $5HT^+$ axonal area (Fig. 6, J to M, and fig. S19C). Subsequently, the motor functional recovery with combination injection was significantly improved compared with those with PBS injection, but neither promoted macrophage migration nor improved functional recovery was observed in combination-injected *IRF8*$^{-/-}$ mice (Fig. 6, J, K and O to Q). These results indicated that the combination promoted IRF8 activation with accelerated macrophage migration into the smaller area during the recovery phase, leading to greater sparing of $5HT^+$ fibers and better functional recovery.

DISCUSSION

In this study, we performed a time-course RNA-seq analysis and identified IRF8 as a contributing factor for SCI recovery. With time-lapse imaging and a histopathological analysis, we revealed that IRF8 was necessary for macrophage-autonomous migration toward high C5a concentrations through the IRF8-purinergic receptor axis, significantly influencing the tissue pathology and functional recovery after SCI. Promoting IRF8 activation enhanced macrophage centripetal migration, leading to improved functional recovery after SCI. These findings shed light on the importance of IRF8-dependent macrophage migration for neurological recovery, raising a possibility of a novel therapeutic strategy for SCI.

Infiltrating macrophages after SCI are considered to have beneficial and detrimental effects. Infiltrating blood-derived macrophages in the lesion epicenter expressed CD11c and had beneficial effects on functional and physiological recovery after SCI (*34*). *IRF8*$^{-/-}$ macrophages that did not reach the epicenter might not express CD11c and have less beneficial effect, leading to worse functional recovery in mice with *IRF8*$^{-/-}$ macrophages. Detrimental effects of macrophages such as promotion of forming scars, damaging axons, and decreasing spared myelin were also shown in several studies using clodronate liposomes for depletion of infiltrating macrophages after SCI (*35*–*37*). *IRF8*$^{-/-}$ macrophages widely scattered in injured spinal cord during recovery phase might exert these detrimental effects on a larger range of spinal cord, resulting in poor functional recovery after SCI. Our results indicate negative correlations between the ranges of macrophages in injured cord and the LFB^+ areas or $GFAP^-$ area (Fig. 4F and fig. S5). Given that the numbers of infiltrating macrophages in WT and *IRF8*$^{-/-}$ mice after SCI are comparable, these results provide a new concept that not only the numbers but also the location of infiltrating macrophages affect remyelination and formation of glial scar. Together, there is a possibility that *IRF8*$^{-/-}$ macrophages with impaired centripetal migration may not express CD11c having less beneficial effects at epicenter and that widely spread *IRF8*$^{-/-}$ macrophages have a detrimental effect over larger areas on injured spinal cord.

In this study, the combination injection of IFN-γ and LPS significantly activated IRF8, but these two molecules would not exist in injured spinal cord without virus or Gram-negative bacteria. Regarding the upstream of IRF8, juxtacrine Jagged1/Notch1 signaling was recently reported to activate IRF8 (*38*, *39*). Macrophages express Jagged1 and Notch1 after CNS injury (*40*), and we confirmed the increased expressions of *Jagged1 and Notch1* in the injured cord (fig. S20A). However, the *Hes1* (target gene of Notch signaling) expression was significantly decreased in macrophages, indicating that Notch signaling was unlikely to be upstream of the IRF8 axis in macrophages after SCI (fig. S20B). We next focused on Toll-like receptor 4 (TLR4) signaling, which is known to induce IRF8 target gene expression in macrophages (*31*). After SCI, necrotizing cells release damage-associated molecular patterns (DAMPs), such as heat shock proteins, high-mobility group box 1 protein, fibronectin and soluble hyaluronan (*41*), and all of which are potential TLR4 ligands that can activate IRF8 signaling (*42*, *43*). We observed a marked increase in the *TLR4* expression on macrophages, suggesting the significance of the DAMP/TLR4/IRF8 pathway for macrophage migration after SCI (fig. S20C).

In an in vitro assay, cultured primary IRF8-deficient microglia derived from the brain show impaired motility accompanied by decreased purinergic receptor expressions, but the relevance of this finding to CNS diseases is not known (*44*). In our study, microglial IRF8–deficient chimeric mice showed that microglial IRF8 has no significant effect on SCI pathology, while purinergic receptors expressed in peripheral blood–derived macrophages via IRF8 caused C5a-directed centripetal migration and significantly affected SCI pathology. These findings demonstrate the possible treatment by enhancing migration of macrophages (Fig. 6 and fig. S2). As Masuda *et al.* (*44*), Davalos *et al.* (*45*), and Haynes *et al.* (*46*) described, microglia in vivo may have difficulty to migrate because of the tight cell adhesion in the tissue after injury, which may be a reason why microglial IRF8 did not significantly affect SCI pathology. These findings suggest the possibility that microglia changes the cell adhesion and motility depending on the surrounding environment by a different mechanism from macrophages.

After IRF8 activation, the macrophages migrated within the C5a gradient (Fig. 5). Regarding the etiology of the C5a gradient, several possible sources may be involved in the injured spinal cord. Immediately after SCI, hemorrhaging and neutrophil infiltration occur at the injury site with blood–spinal cord barrier disruption (*4*, *47*). In this phase, massive C5a flows directly into the lesion area from the peripheral blood, and infiltrating neutrophils also produce C5a (fig. S21A) (*47*). In addition, the pericytes that increase in number at the center of the lesion after SCI may also express C5a (fig. S21B) (*48*, *49*). Furthermore, macrophages themselves also expressed C5a after migrating near the epicenter (fig. S21C). As a consequence, a C5a gradient was orchestrated around the lesion, gradually guiding the macrophages to the epicenter. Roach *et al.* (*50*) discovered that C5a binds to G protein–coupled receptors of macrophages and increases intercellular concentration of $Ca2^+$ via PLCβ3 dependent on $G\alpha_i$. Considering that the increase of Ca^{2+} intracellular concentration causes the exocytosis of ATP, released ATP by exocytosis via the C5a–G protein coupling receptor–PLCβ3 axis could bind to purinergic receptors, leading to promote macrophagic migration (*51*, *52*).

Among the C5a gradient, WT macrophages migrated to epicenter leading to the remyelination, while *IRF8*$^{-/-}$ macrophages remain widely spread over the lesion with the large demyelinated area after SCI (Figs. 3 and 5). This profound demyelination at 42 dpi might be due to possible severe initial demyelination caused by acute inflammation after SCI (*4*). However, there were no significant differences in cell numbers and inflammatory cytokine expression levels between WT and *IRF8*$^{-/-}$ macrophages (Fig. 3, A and B, and figs. S1 and S13 to S15). Although IRF8 was suggested to be involved with inflammation in certain environments (*39*), considering that inflammatory cytokine expression in infiltrating macrophages peaked around

12 hours after SCI and thereafter notably decreased at 4 and 7 dpi (*24*), IRF8 that activates after 7 dpi could not regulate these inflammatory cytokines after SCI (Fig. 2B). With the comparable inflammatory reaction, *IRF8*$^{-/-}$ mice showed similar initial demyelinated area in acute phase compared with WT mice, indicating that the large demyelinated area in *IRF8*$^{-/-}$ mice at 42 dpi was due to impaired remyelination process (fig. S5).

After SCI, axons in spinal tracts retract away from the injury site, and this deleterious phenomenon is known as axonal dieback (*53*). Since the spared axon is indispensable for the remyelination process, which is important for functional recovery, reducing axonal dieback could be a promising therapeutic strategy for SCI (*22*). As the primary mechanism of the axonal dieback, it was demonstrated that macrophages in contact with axons caused the axonal dieback via macrophage-derived matrix metalloproteinases (*7*). In vivo time-lapse multiphoton imaging showed that this macrophage-mediated axonal dieback occurs in the area where infiltrating macrophages were present until at least 3 weeks after SCI (*8*). Considering that the combination injection facilitated the macrophage migration to the compacted area over this time period, the larger amount of axons escaped from the contact with macrophages as well as the axonal dieback, resulting in the improved functional recovery in the treatment group (Fig. 6, G to Q). IFN-γ is therapeutically used for patients with renal cancer, chronic granulomatous disease, and Sézary syndrome, and LPS is also used in infection prevention (*54*–*57*). We also confirmed that there was no detrimental effect with the combination using IFN-γ and LPS in the subacute phase of SCI (fig. S19, A and B), suggesting the high feasibility of this novel therapeutic strategy via IRF8 activation (*31*).

Although the distribution of *IRF8*$^{-/-}$ macrophages was wider than that of WT macrophages, some macrophages were near the epicenter at 14 and 42 dpi (Fig. 3, C and E). This suggests the possibility that, in addition to IRF8, other molecules might be also involved in migration of macrophages in the injured spinal cord. Following this study, to discover and investigate these molecules would lead to a better understanding of the mechanism underlying macrophage migration after SCI.

In conclusion, we demonstrated that lack of epicenter-directed macrophage migration led to worse functional recovery after SCI. IRF8 drives macrophage migration toward C5a, regulating the purinergic receptor expression. Our findings provide deeper insight into the role of macrophage centripetal movement in spontaneous recovery, providing the therapeutic potential of promoting infiltrating cell migration toward the lesion epicenter after traumatic CNS injury.

MATERIALS AND METHODS

Animals

All study protocols involving mice were approved by the Committee of Ethics on Animal Experimentation of our institution and conducted in accordance with the National Institutes of Health guidelines for the care and use of animals. All mice were housed in a temperature- and humidity-controlled environment on a 12-hour light-dark cycle and food/water available ad libitum. *IRF8*$^{-/-}$ and *Nes-EGFP*$^{+}$ mice were generated as described previously (*9*, *17*). To generate *IRF8*$^{-/-}$*;EGFP*$^{+}$ mice, we crossed *IRF8*$^{-/-}$ and *CAG-EGFP* mice. Bone marrow transplantation was performed as previously described (*20*). Eight-week-old female C57BL/6 J mice were used as WT mice. Microglial IRF8–deficient chimeric mice were generated by transferring the bone marrow cells (BMCs) of EGFP^{+} *IRF8*$^{+/+}$ mice into *IRF8*$^{-/-}$ recipient mice, and macrophagic IRF8–deficient chimeric mice were generated by transferring the BMCs of EGFP^{+} *IRF8*$^{-/-}$ mice into WT recipient mice after irradiation, as previously described (*20*). Accordingly, the former mice consisted of EGFP^{+} *IRF8*$^{+/+}$ macrophages and EGFP^{-} *IRF8*$^{-/-}$ microglia, while the latter consisted of EGFP^{+} *IRF8*$^{-/-}$ macrophages and EGFP^{-} *IRF8*$^{+/+}$ microglia. In these chimeric mice, macrophages were distinguished from microglia by their potent EGFP expression. [EGFP^{+} macrophages: *IRF8*$^{+/+}$]/[EGFP^{-} microglia: *IRF8*$^{+/+}$] mice were generated by transferring EGFP^{+} *IRF8*$^{+/+}$ BMCs into *IRF8*$^{+/+}$ recipient mice, and [*EGFP*$^{+}$ macrophages: *IRF8*$^{-/-}$]/[microglia: *IRF8*$^{+/+}$] mice were generated by transferring EGFP^{+} *IRF8*$^{-/-}$ BMCs into *IRF8*$^{+/+}$ mice.

Spinal cord injury

The mice were anesthetized with pentobarbital (75 mg/kg intraperitoneally) and subjected to a contusion injury (70 kilodynes) at the 10th thoracic level using an Infinite Horizons Impactor (Precision Systems Instrumentation) (*15*). After injury, the overlying muscles were sutured, and the skin was closed with wound clips. During the period of recovery from anesthesia, the animals were placed in a temperature-controlled chamber until thermoregulation was re-established. The motor function was evaluated according to a locomotor open-field rating scale, the BMS (*58*). A footprint analysis was performed as previously described (*24*). The forelimbs and hindlimbs of the mice were dipped in red and green dyes, respectively. For the grip walk test, each mouse was evaluated using 50 cm of the grid with three patterns: easy (50 steps, 1 cm apart), medium (every third step removed), and hard (every other step removed) (*25*). The sum of the number of grips for all three patterns was used in the analysis. A team of two experienced examiners evaluated the score of each animal in a blinded fashion (*32*).

C5a injection

A glass tip was inserted 2 mm rostral and caudal from the epicenter of the injured spinal cord, and 2 μl of 1 μM mouse recombinant C5a (R&D Systems) was injected at 0.5 μl/min using a stereotaxic injector (KDS 310, Muromachi Kikai) from 4 to 7 dpi (*14*). Control animals received 2 μl of PBS from 4 to 7 dpi.

Macrophage transplantation

Using flow cytometry, macrophages with or without IRF8 activation were obtained from the injured spinal cord of bone marrow chimeric mice [EGFP^{+} macrophages: *IRF8*$^{+/+}$]/[microglia: *IRF8*$^{+/+}$] at 7 or 4 dpi. EGFP^{+} cells (5.0×10^{5}) were transplanted into the injured spinal cord of WT mice immediately after SCI using a glass micropipette and a stereotaxic injector, as described previously (KDS 310, Muromachi Kikai) (*6*). Injections were performed bilaterally at four sites of intact parenchyma 1.5 mm rostral and caudal to the epicenter.

Combination administration

Injured mice received an injection of 2 μg of recombinant murine IFN-γ (PeproTech) and 200 ng of LPS (Sigma-Aldrich) at the epicenter using a stereotaxic injector (KDS 310, Muromachi Kikai) every 2 days from 2 dpi. For in vitro combination administration, 10 ng of IFN-γ and 100 ng of LPS were added to macrophages (4.0×10^{4}/ml) differentiated from WT CD11b^{+}/Ly6G^{-}/CD45^{high} peripheral blood–derived monocytes after cultivated for 4 days as previously

described (*59*), and an immunocytochemical analysis and mRNA extraction were performed at 3 hours after stimulation, respectively. The paw withdrawal threshold was analyzed as previously described (*19*).

In vivo cocktail block

Injured mice received an injection of 10 μM AR-C69931MX (R&D Systems), 10 μM AR-C 118925XX (R&D Systems), 100 μM 8-SPT (Santa Cruz Biotechnology), 100 μM MRS-2179 (Cayman Chemical), and 300 nM NF-449 (Cayman Chemical) at the epicenter using a stereotaxic injector every 2 days from 4 to 14 dpi.

Histopathological examination

The animals were reanesthetized and transcardially fixed with 4% paraformaldehyde. The spinal cord was removed, dehydrated, and embedded in an optimal cutting temperature compound, and frozen sections were cut on a cryostat in the sagittal plane at 14 mm. The sections were subsequently stained with primary antibodies at 4°C overnight and then incubated with Alexa Fluor secondary antibodies (1:200; Invitrogen) and Hoechst 33258. LFB-stained serial sections were evaluated as previously described (*4*, *9*, *15*). The R.T.U. (Ready-to-Use) Vectastain kit (Vector Laboratories) was used for CD68 staining (*15*). The following primary antibodies were used: CD68 (rat, MCA1957; 1:200; Serotec), GFAP (rabbit, Z0334; 1:200; Dako), IRF8 (goat, sc-6058; 1:200; Santa Cruz Biotechnology), GST-π (mouse, no. 610719; 1:200; BD Biosciences), NeuN (mouse, MAB377; 1:200; Chemicon), PMN (rat, MCA771GA; 1:200; Serotec), CD3 (145-2C11; 1:200; eBioscience), 5-HT (goat, no.20079; 1:200; ImmunoStar), platelet-derived growth factor receptor-β (PDGFRβ) (rat, no.136002; 1:200; BioLegend), and C5a (rabbit, BS-0324R; 1:200; Bioss). Infiltrating macrophages change their morphology to the amoeboid form in injured tissue (*4*, *60*, *61*). The range of morphologically amoeboid CD68 macrophages and $5HT^+$ area was measured using the BZ-II analyzer software program (Keyence). All images were captured using a BZ-9000 digital microscope system (Keyence), EVOS microscope (Life Technologies), or epifluorescence microscope equipped with a digital camera (BX51, Olympus).

Flow cytometry

The spinal cords (6.0 mm in length, centered around the lesion) were dissociated in collagenase type I (Invitrogen) and stained with antibodies, as previously described (*4*). The samples were analyzed using a FACSAria II flow cytometer and the FACSDiva software program (BD Biosciences). The following antibodies were used: PE-Cy7–conjugated CD45 (30-F11; 1:10), APC-conjugated CD11b (M1/70; 1:10), fluorescein isothiocyanate–conjugated CD11b (M1/70; 1:10), APC-conjugated CD11b (M1/70; 1:10), PE-conjugated Ly6G (1A8; 1:50), APC-conjugated Ly6C (HK1.4; 1:10), PE-conjugated F4/80 (BM8; 1:10), biotin-conjugated CD115 (AFS98; 1:10), and Streptavidin-PerCP-Cyanine5.5 (45-4317-80; 1:10). All conjugated antibodies were purchased from eBioscience. CD45 is a marker of myeloid cells. In the injured spinal cord, infiltrating macrophages are divided into $CD45^{high}$ population (*4*). CD11b is a marker for macrophages, monocytes, and neutrophils (*4*). Ly6G is a marker for neutrophils (*6*). We isolated $CD11b^{high}/Ly6G^{nega}/CD45^{high}$ population as infiltrating macrophages (*4*, *6*, *15*). Ly6C is a marker for a subset of macrophages (*6*, *18*). CD115 is a marker for monocytes (*18*). We isolated $EGFP^+/CD11b^{posi}/Ly6G^{nega}/CD115^{posi}$ population as peripheral blood–derived monocytes from $EGFP^+$ bone marrow chimeric mice. Reactive astrocytes isolated from the spinal cords of *Nes-EGFP*$^+$ mice were used as the $EGFP^+$ population. Isolated macrophages or reactive astrocytes were either subjected to RNA extraction or incubated in Dulbecco's modified Eagle's medium for transplantation and in vitro combination administration.

Laser microdissection

As previously described (*62*), fresh injured spinal cords were immediately frozen in dry ice/hexane and stored in a deep freezer at −80°C. The tissues were sectioned into 16-μm-thick slices using a cryostat at −20°C and were mounted on polyethylene naphthalate (PEN) membrane slides. The sections were then fixed in ice-cold acetone for 2 min. Astrocytes were obtained from injured spinal cords of *Nes-EGFP*$^+$ mice, which have $EGFP^+$-reactive astrocytes after SCI as described previously (*9*). For neurons, sections were fixed for 10 s in 75% EtOH, stained for 30 s in 4% cresyl violet acetate/0.3% acetic acid, and dehydrated in graded solutions of ethanol (70, 95, and 100%), followed by 45 s in xylene (*63*). $EGFP^+$ astrocytes or stained neurons were dissected with an LMD 6500 system (Leica Microsystems) and were transferred by gravity into a microcentrifuge tube cap placed directly beneath the section. The tube cap was filled with 75 μl of buffer RLT (Qiagen). For each sample, 500 cells were dissected from one series of sagittal sections.

Quantitative RT-PCR

Total RNA was isolated from the macrophages obtained from the spinal cord tissue using the RNeasy Micro Kit (Qiagen) or from the injured spinal cord (4 mm or 500 μm in length) using the RNeasy Mini Kit (Qiagen). The total RNA of reactive astrocytes and neurons was selectively isolated with LMD as previously described (*14*, *62*, *63*). For the complementary DNA synthesis, a reverse transcription reaction was performed using PrimeScript Reverse Transcriptase (Takara). qPCR was performed using primers specific to the genes of interest (table S1) and SYBR Premix DimerEraser (Takara). The data were normalized to the expression level of glyceraldehyde-3-phosphate dehydrogenase.

RNA sequencing

The sample preparation and data analysis were performed as described previously (*64*). Briefly, the mRNA sequencing library was prepared using the NEBNext Ultra Directional Library Prep Kit for Illumina (New England Biolabs), and the samples were sequenced on an Illumina HiSeq 1500 system. The gene expression levels (FPKM) were calculated using the TopHat (version 2.0.11) and Cufflinks (version 2.1.1) software programs with default parameters (*16*). An enrichment analysis for the biological processes was performed based on the GO database annotations with DAVID (*65*). The calculated −ln(*P* values) were displayed on the *x* axis of the graph.

Chemotaxis assays

Time-lapse imaging of WT and *IRF8*$^{-/-}$ macrophages was performed as described previously (*28*). Briefly, macrophages obtained from WT or *IRF8*$^{-/-}$ mice were labeled with PE-conjugated F4/80 (a marker for mouse macrophages) antibody, and $F4/80^+$ cells were isolated using FACSAria II. These macrophages were resuspended in 100 to 150 μl of RPMI 1640 containing bicarbonate and 10% fetal calf serum (FCS), and 8 μl of the suspension was seeded into the narrow channel of an uncoated (ibiTreat) μ-slide chemotaxis chamber (Ibidi) placed in a humidified incubator (at 37°C with 5% CO_2). This narrow channel (observation area)

connects two 40-ml reservoirs. In the chemotaxis experiments, bicarbonate-free RPMI 1640 containing 20 mM Hepes (Biochrom AG) and 10% FCS was used. A final concentration of 10 nM mouse recombinant C5a was added to one of the reservoirs, and the cells were imaged by phase-contrast microscopy. Images were captured every 10 min for 18 hours, and the cell migration tracks between 8 and 18 hours were analyzed using the ImageJ software program (National Institutes of Health) with a manual tracking plug-in and the chemotaxis and migration tool from Ibidi. Eighteen randomly selected cells were tracked in each chemotaxis experiment.

Statistical analysis

The Wilcoxon rank-sum test was used to compare the medians of the data for qPCR as well as the cell count, craniocaudal range of macrophages, and functional outcome score. For multiple comparisons in qPCR, Dunnett's test was applied. For the analysis of the differences in the BMS scores between the groups over time, a two-way repeated-measures ANOVA with post hoc Tukey's test was performed. For the comparative analysis of three or more groups, a one-way ANOVA with post hoc Tukey's test was performed. All tests were two sided, and the level of significance was set at 0.05. The values for groups were presented as the average ± SEM. All statistical analyses were carried out using the JMP software program (version 13; SAS Institute).

SUPPLEMENTARY MATERIALS

Supplementary material for this article is available at http://advances.sciencemag.org/cgi/content/full/5/5/eaav5086/DC1

Fig. S1. Comparable numbers of microglia, Ly6C^{high} and Ly6C^{low} populations, and gene expression levels of M1/M2 markers in macrophages between WT and *IRF8*$^{-/-}$ mice after SCI.
Fig. S2. The microglial IRF8–deficient does not affect CD68^{+} macrophage migration and functional recovery after SCI.
Fig. S3. Gating for EGFP^{+} peripheral blood monocytes.
Fig. S4. Macrophages infiltrated into the injured spinal cord by 3 dpi.
Fig. S5. Widespread *IRF8*$^{-/-}$ macrophage with few 5HT^{+} axons, leading to less demyelination after SCI.
Fig. S6. KEGG pathway analysis detected six cytokine-related pathways in analysis with RNA-seq data of 4, 7, and 14 dpi.
Fig. S7. IRF8 has no significant influence on expression levels of genes present in the cytokine-cytokine receptor interaction of KEGG pathway after SCI.
Fig. S8. IRF8 has no significant influence on expression levels of genes present in the nuclear factor κB signaling pathway of KEGG pathway after SCI.
Fig. S9. IRF8 has no significant influence on expression levels of genes present in the chemokine signaling pathway of KEGG pathway after SCI.
Fig. S10. IRF8 has no significant influence on expression levels of genes present in the TLR signaling pathway of KEGG pathway after SCI.
Fig. S11. IRF8 has no significant influence on expression levels of genes present in the transforming growth factor–β signaling pathway of KEGG pathway after SCI.
Fig. S12. IRF8 has no significant influence on expression levels of genes present in the TNF signaling pathway of KEGG pathway after SCI.
Fig. S13. Gene expression levels of cytokines in WT and *IRF8*$^{-/-}$ macrophages.
Fig. S14. Gene expression levels of cytokines in WT and *IRF8*$^{-/-}$ macrophages at 7 dpi.
Fig. S15. Gene expression levels of cytokines in WT and *IRF8*$^{-/-}$ macrophages at 14 dpi.
Fig. S16. The failure of centripetal migration of macrophages led to a wide range of neuronal loss after SCI.
Fig. S17. IRF8 did not significantly influence expression of C5a receptors of macrophages after SCI.
Fig. S18. EGFP^{+} macrophages at 1 hour after transplantation.
Fig. S19. Promoting IRF8 had no harmful effect on the systemic inflammatory response after SCI.
Fig. S20. TLR4 signaling of macrophages was activated after SCI.
Fig. S21. Sources of C5a in injured spinal cord.
Table S1. Primers used for qPCR.
Movie S1. Chemotaxis assay of WT macrophages.
Movie S2. Chemotaxis assay of *IRF8*$^{-/-}$ macrophages.

REFERENCES AND NOTES

1. J. W. McDonald, C. Sadowsky, Spinal-cord injury. *Lancet* **359**, 417–425 (2002).
2. S. L. Carlson, M. E. Parrish, J. E. Springer, K. Doty, L. Dossett, Acute inflammatory response in spinal cord following impact injury. *Exp. Neurol.* **151**, 77–88 (1998).
3. S. David, A. Kroner, Repertoire of microglial and macrophage responses after spinal cord injury. *Nat. Rev. Neurosci.* **12**, 388–399 (2011).
4. H. Saiwai, Y. Ohkawa, H. Yamada, H. Kumamaru, A. Harada, H. Okano, T. Yokomizo, Y. Iwamoto, S. Okada, The LTB4-BLT1 axis mediates neutrophil infiltration and secondary injury in experimental spinal cord injury. *Am. J. Pathol.* **176**, 2352–2366 (2010).
5. C. A. Iannotti, M. Clark, K. P. Horn, N. van Rooijen, J. Silver, M. P. Steinmetz, A combination immunomodulatory treatment promotes neuroprotection and locomotor recovery after contusion SCI. *Exp. Neurol.* **230**, 3–15 (2011).
6. H. Saiwai, H. Kumamaru, Y. Ohkawa, K. Kubota, K. Kobayakawa, H. Yamada, T. Yokomizo, Y. Iwamoto, S. Okada, Ly6C^{+} Ly6G^{-} Myeloid-derived suppressor cells play a critical role in the resolution of acute inflammation and the subsequent tissue repair process after spinal cord injury. *J. Neurochem.* **125**, 74–88 (2013).
7. S. A. Busch, K. P. Horn, D. J. Silver, J. Silver, Overcoming macrophage-mediated axonal dieback following CNS injury. *J. Neurosci.* **29**, 9967–9976 (2009).
8. T. A. Evans, D. S. Barkauskas, J. T. Myers, E. G. Hare, J. Q. You, R. M. Ransohoff, A. Y. Huang, J. Silver, High-resolution intravital imaging reveals that blood-derived macrophages but not resident microglia facilitate secondary axonal dieback in traumatic spinal cord injury. *Exp. Neurol.* **254**, 109–120 (2014).
9. S. Okada, M. Nakamura, H. Katoh, T. Miyao, T. Shimazaki, K. Ishii, J. Yamane, A. Yoshimura, Y. Iwamoto, Y. Toyama, H. Okano, Conditional ablation of Stat3 or Socs3 discloses a dual role for reactive astrocytes after spinal cord injury. *Nat. Med.* **12**, 829–834 (2006).
10. E. S. Rosenzweig, G. Courtine, D. L. Jindrich, J. H. Brock, A. R. Ferguson, S. C. Strand, Y. S. Nout, R. R. Roy, D. M. Miller, M. S. Beattie, L. A. Havton, J. C. Bresnahan, V. R. Edgerton, M. H. Tuszynski, Extensive spontaneous plasticity of corticospinal projections after primate spinal cord injury. *Nat. Neurosci.* **13**, 1505–1510 (2010).
11. Z. Wang, M. Gerstein, M. Snyder, RNA-Seq: A revolutionary tool for transcriptomics. *Nat. Rev. Genet.* **10**, 57–63 (2009).
12. H. Lörchner, J. Pöling, P. Gajawada, Y. Hou, V. Polyakova, S. Kostin, J. M. Adrian-Segarra, T. Boettger, A. Wietelmann, H. Warnecke, M. Richter, T. Kubin, T. Braun, Myocardial healing requires Reg3β-dependent accumulation of macrophages in the ischemic heart. *Nat. Med.* **21**, 353–362 (2015).
13. C. S. Grasso, Y. Tang, N. Truffaux, N. E. Berlow, L. Liu, M.-A. Debily, M. J. Quist, L. E. Davis, E. C. Huang, P. J. Woo, A. Ponnuswami, S. Chen, T. B. Johung, W. Sun, M. Kogiso, Y. du, L. Qi, Y. Huang, M. Hütt-Cabezas, K. E. Warren, L. le Dret, P. S. Meltzer, H. Mao, M. Quezado, D. G. van Vuurden, J. Abraham, M. Fouladi, M. N. Svalina, N. Wang, C. Hawkins, J. Nazarian, M. M. Alonso, E. H. Raabe, E. Hulleman, P. T. Spellman, X.-N. Li, C. Keller, R. Pal, J. Grill, M. Monje, Functionally defined therapeutic targets in diffuse intrinsic pontine glioma. *Nat. Med.* **21**, 555–559 (2015).
14. H. Kumamaru, Y. Ohkawa, H. Saiwai, H. Yamada, K. Kubota, K. Kobayakawa, K. Akashi, H. Okano, Y. Iwamoto, S. Okada, Direct isolation and RNA-seq reveal environment-dependent properties of engrafted neural stem/progenitor cells. *Nat. Commun.* **3**, 1140 (2012).
15. K. Kobayakawa, H. Kumamaru, H. Saiwai, K. Kubota, Y. Ohkawa, J. Kishimoto, K. Yokota, R. Ideta, K. Shiba, H. Tozaki-Saitoh, K. Inoue, Y. Iwamoto, S. Okada, Acute hyperglycemia impairs functional improvement after spinal cord injury in mice and humans. *Sci. Transl. Med.* **6**, 256ra137 (2014).
16. C. Trapnell, A. Roberts, L. Goff, G. Pertea, D. Kim, D. R. Kelley, H. Pimentel, S. L. Salzberg, J. L. Rinn, L. Pachter, Differential gene and transcript expression analysis of RNA-seq experiments with TopHat and Cufflinks. *Nat. Protoc.* **7**, 562–578 (2012).
17. T. Holtschke, J. Löhler, Y. Kanno, T. Fehr, N. Giese, F. Rosenbauer, J. Lou, K. P. Knobeloch, L. Gabriele, J. F. Waring, M. F. Bachmann, R. M. Zinkernagel, H. C. Morse III, K. Ozato, I. Horak, Immunodeficiency and chronic myelogenous leukemia-like syndrome in mice with a targeted mutation of the ICSBP gene. *Cell* **87**, 307–317 (1996).
18. R. Shechter, O. Miller, G. Yovel, N. Rosenzweig, A. London, J. Ruckh, K.-W. Kim, E. Klein, V. Kalchenko, P. Bendel, S. A. Lira, S. Jung, M. Schwartz, Recruitment of beneficial M2 macrophages to injured spinal cord is orchestrated by remote brain choroid plexus. *Immunity* **38**, 555–569 (2013).
19. T. Masuda, M. Tsuda, R. Yoshinaga, H. Tozaki-Saitoh, K. Ozato, T. Tamura, K. Inoue, IRF8 is a critical transcription factor for transforming microglia into a reactive phenotype. *Cell Rep.* **1**, 334–340 (2012).
20. A. Rolls, R. Shechter, A. London, Y. Segev, J. Jacob-Hirsch, N. Amariglio, G. Rechavi, M. Schwartz, Two faces of chondroitin sulfate proteoglycan in spinal cord repair: A role in microglia/macrophage activation. *PLOS Med.* **5**, e171 (2008).
21. C. Morganti-Kossmann, R. Raghupathi, A. I. R. Maas, *Traumatic Brain and Spinal Cord Injury: Challenges and Developments* (Cambridge Univ. Press, 2012), pp. xiii.
22. R. J. M. Franklin, C. Ffrench-Constant, Remyelination in the CNS: From biology to therapy. *Nat. Rev. Neurosci.* **9**, 839–855 (2008).

23. Q. Cao, Y. P. Zhang, C. Iannotti, W. H. DeVries, X.-M. Xu, C. B. Shields, S. R. Whittemore, Functional and electrophysiological changes after graded traumatic spinal cord injury in adult rat. *Exp. Neurol.* **191** (Suppl 1), S3–S16 (2005).
24. H. Kumamaru, H. Saiwai, Y. Ohkawa, H. Yamada, Y. Iwamoto, S. Okada, Age-related differences in cellular and molecular profiles of inflammatory responses after spinal cord injury. *J. Cell. Physiol.* **227**, 1335–1346 (2012).
25. A. Pajoohesh-Ganji, K. R. Byrnes, G. Fatemi, A. I. Faden, A combined scoring method to assess behavioral recovery after mouse spinal cord injury. *Neurosci. Res.* **67**, 117–125 (2010).
26. H. Ogata, S. Goto, K. Sato, W. Fujibuchi, H. Bono, M. Kanehisa, KEGG: Kyoto Encyclopedia of Genes and Genomes. *Nucleic Acids Res.* **27**, 29–34 (1999).
27. J. G. McComb, M. Ranganathan, X. H. Liu, J. M. Pilewski, P. Ray, S. C. Watkins, A. M. K. Choi, J. S. Lee, CX3CL1 up-regulation is associated with recruitment of CX3CR1$^+$ mononuclear phagocytes and T lymphocytes in the lungs during cigarette smoke-induced emphysema. *Am. J. Pathol.* **173**, 949–961 (2008).
28. M. Kronlage, J. Song, L. Sorokin, K. Isfort, T. Schwerdtle, J. Leipziger, B. Robaye, P. B. Conley, H.-C. Kim, S. Sargin, P. Schön, A. Schwab, P. J. Hanley, Autocrine purinergic receptor signaling is essential for macrophage chemotaxis. *Sci. Signal.* **3**, ra55 (2010).
29. A. Gorelik, T. Sapir, R. Haffner-Krausz, T. Olender, T. M. Woodruff, O. Reiner, Developmental activities of the complement pathway in migrating neurons. *Nat. Commun.* **8**, 15096 (2017).
30. N.-J. Chen, C. Mirtsos, D. Suh, Y.-C. Lu, W.-J. Lin, C. McKerlie, T. Lee, H. Baribault, H. Tian, W.-C. Yeh, C5L2 is critical for the biological activities of the anaphylatoxins C5a and C3a. *Nature* **446**, 203–207 (2007).
31. J. Zhao, H. J. Kong, H. Li, B. Huang, M. Yang, C. Zhu, M. Bogunovic, F. Zheng, L. Mayer, K. Ozato, J. Unkeless, H. Xiong, IRF-8/interferon (IFN) consensus sequence-binding protein is involved in Toll-like receptor (TLR) signaling and contributes to the cross-talk between TLR and IFN-gamma signaling pathways. *J. Biol. Chem.* **281**, 10073–10080 (2006).
32. H. Kumamaru, H. Saiwai, K. Kubota, K. Kobayakawa, K. Yokota, Y. Ohkawa, K. Shiba, Y. Iwamoto, S. Okada, Therapeutic activities of engrafted neural stem/precursor cells are not dormant in the chronically injured spinal cord. *Stem Cells* **31**, 1535–1547 (2013).
33. D. Gris, E. F. Hamilton, L. C. Weaver, The systemic inflammatory response after spinal cord injury damages lungs and kidneys. *Exp. Neurol.* **211**, 259–270 (2008).
34. R. Shechter, A. London, C. Varol, C. Raposo, M. Cusimano, G. Yovel, A. Rolls, M. Mack, S. Pluchino, G. Martino, S. Jung, M. Schwartz, Infiltrating blood-derived macrophages are vital cells playing an anti-inflammatory role in recovery from spinal cord injury in mice. *PLOS Med.* **6**, e1000113 (2009).
35. S. M. Lee, S. Rosen, P. Weinstein, N. van Rooijen, L. J. Noble-Haeusslein, Prevention of both neutrophil and monocyte recruitment promotes recovery after spinal cord injury. *J. Neurotrauma* **28**, 1893–1907 (2011).
36. Y.-S. Lee, L. H. Funk, J. K. Lee, M. B. Bunge, Macrophage depletion and Schwann cell transplantation reduce cyst size after rat contusive spinal cord injury. *Neural Regen. Res.* **13**, 684–691 (2018).
37. Y. Zhu, C. Soderblom, V. Krishnan, J. Ashbaugh, J. R. Bethea, J. K. Lee, Hematogenous macrophage depletion reduces the fibrotic scar and increases axonal growth after spinal cord injury. *Neurobiol. Dis.* **74**, 114–125 (2015).
38. J. Foldi, A. Y. Chung, H. Xu, J. Zhu, H. H. Outtz, J. Kitajewski, Y. Li, X. Hu, L. B. Ivashkiv, Autoamplification of Notch signaling in macrophages by TLR-induced and RBP-J-dependent induction of Jagged1. *J. Immunol.* **185**, 5023–5031 (2010).
39. H. Xu, J. Zhu, S. Smith, J. Foldi, B. Zhao, A. Y. Chung, H. Outtz, J. Kitajewski, C. Shi, S. Weber, P. Saftig, Y. Li, K. Ozato, C. P. Blobel, L. B. Ivashkiv, X. Hu, Notch-RBP-J signaling regulates the transcription factor IRF8 to promote inflammatory macrophage polarization. *Nat. Immunol.* **13**, 642–650 (2012).
40. M. F. Stidworthy, S. Genoud, W.-W. Li, D. P. Leone, N. Mantei, U. Suter, R. J. Franklin, Notch1 and Jagged1 are expressed after CNS demyelination, but are not a major rate-determining factor during remyelination. *Brain* **127**, 1928–1941 (2004).
41. K. H. Mills, TLR-dependent T cell activation in autoimmunity. *Nat. Rev. Immunol.* **11**, 807–822 (2011).
42. K. A. Kigerl, P. G. Popovich, Toll-like receptors in spinal cord injury. *Curr. Top. Microbiol. Immunol.* **336**, 121–136 (2009).
43. K. Ohashi, V. Burkart, S. Flohé, H. Kolb, Cutting edge: Heat shock protein 60 is a putative endogenous ligand of the toll-like receptor-4 complex. *J. Immunol.* **164**, 558–561 (2000).
44. T. Masuda, N. Nishimoto, D. Tomiyama, T. Matsuda, H. Tozaki-Saitoh, T. Tamura, S. Kohsaka, M. Tsuda, K. Inoue, IRF8 is a transcriptional determinant for microglial motility. *Purinergic Signal.* **10**, 515–521 (2014).
45. D. Davalos, J. Grutzendler, G. Yang, J. V. Kim, Y. Zuo, S. Jung, D. R. Littman, M. L. Dustin, W.-B. Gan, ATP mediates rapid microglial response to local brain injury in vivo. *Nat. Neurosci.* **8**, 752–758 (2005).
46. S. E. Haynes, G. Hollopeter, G. Yang, D. Kurpius, M. E. Dailey, W. B. Gan, D. Julius, The P2Y12 receptor regulates microglial activation by extracellular nucleotides. *Nat. Neurosci.* **9**, 1512–1519 (2006).
47. S. L. Peterson, A. J. Anderson, Complement and spinal cord injury: Traditional and non-traditional aspects of complement cascade function in the injured spinal cord microenvironment. *Exp. Neurol.* **258**, 35–47 (2014).
48. C. Göritz, D. O. Dias, N. Tomilin, M. Barbacid, O. Shupliakov, J. Frisen, A pericyte origin of spinal cord scar tissue. *Science* **333**, 238–242 (2011).
49. Y. Zhang, K. Chen, S. A. Sloan, M. L. Bennett, A. R. Scholze, S. O'Keeffe, H. P. Phatnani, P. Guarnieri, C. Caneda, N. Ruderisch, S. Deng, S. A. Liddelow, C. Zhang, R. Daneman, T. Maniatis, B. A. Barres, J. Q. Wu, An RNA-sequencing transcriptome and splicing database of glia, neurons, and vascular cells of the cerebral cortex. *J. Neurosci.* **34**, 11929–11947 (2014).
50. T. I. A. Roach, R. A. Rebres, I. D. C. Fraser, D. L. DeCamp, K.-M. Lin, P. C. Sternweis, M. I. Simon, W. E. Seaman, Signaling and cross-talk by C5a and UDP in macrophages selectively use PLCbeta3 to regulate intracellular free calcium. *J. Biol. Chem.* **283**, 17351–17361 (2008).
51. E. R. Lazarowski, Vesicular and conductive mechanisms of nucleotide release. *Purinergic Signal.* **8**, 359–373 (2012).
52. R. D. Burgoyne, A. Morgan, Secretory granule exocytosis. *Physiol. Rev.* **83**, 581–632 (2003).
53. C. E. Hill, A view from the ending: Axonal dieback and regeneration following SCI. *Neurosci. Lett.* **652**, 11–24 (2017).
54. J. E. Pennington, Lipopolysaccharide Pseudomonas Vaccine: Efficacy Against Pulmonary Infection with Pseudomonas aeruginosa. *J. Infect. Dis.* **140**, 73–80 (1979).
55. W. Aulitzky, G. Gastl, W. E. Aulitzky, M. Herold, J. Kemmler, B. Mull, J. Frick, C. Huber, Successful treatment of metastatic renal cell carcinoma with a biologically active dose of recombinant interferon-gamma. *J. Clin. Oncol.* **7**, 1875–1884 (1989).
56. B. E. Marciano, R. Wesley, E. S. de Carlo, V. L. Anderson, L. A. Barnhart, D. Darnell, H. L. Malech, J. I. Gallin, S. M. Holland, Long-term interferon-γ therapy for patients with chronic granulomatous disease. *Clin. Infect. Dis.* **39**, 692–699 (2004).
57. K. S. McGinnis, R. Ubriani, S. Newton, J. M. Junkins-Hopkins, C. C. Vittorio, E. J. Kim, M. Wysocka, A. H. Rook, The addition of interferon gamma to oral bexarotene therapy with photopheresis for Sézary syndrome. *Arch. Dermatol.* **141**, 1176–1178 (2005).
58. M. Ma, D. M. Basso, P. Walters, B. T. Stokes, L. B. Jakeman, Behavioral and histological outcomes following graded spinal cord contusion injury in the C57Bl/6 mouse. *Exp. Neurol.* **169**, 239–254 (2001).
59. A. Johansson, C. Dahlgren, Differentiation of human peripheral blood monocytes to macrophages is associated with changes in the cellular respiratory burst activity. *Cell Biochem. Funct.* **10**, 87–93 (1992).
60. P. Friedl, B. Weigelin, Interstitial leukocyte migration and immune function. *Nat. Immunol.* **9**, 960–969 (2008).
61. C. Vérollet, G. M. Charrière, A. Labrousse, C. Cougoule, V. le Cabec, I. Maridonneau-Parini, Extracellular proteolysis in macrophage migration: Losing grip for a breakthrough. *Eur. J. Immunol.* **41**, 2805–2813 (2011).
62. K. Yokota, K. Kobayakawa, K. Kubota, A. Miyawaki, H. Okano, Y. Ohkawa, Y. Iwamoto, S. Okada, Engrafted neural stem/progenitor cells promote functional recovery through synapse reorganization with spared host neurons after spinal cord injury. *Stem Cell Reports* **5**, 264–277 (2015).
63. C. S. Lobsiger, S. Boillée, D. W. Cleveland, Toxicity from different SOD1 mutants dysregulates the complement system and the neuronal regenerative response in ALS motor neurons. *Proc. Natl. Acad. Sci. U.S.A.* **104**, 7319–7326 (2007).
64. A. Harada, K. Maehara, Y. Sato, D. Konno, T. Tachibana, H. Kimura, Y. Ohkawa, Incorporation of histone H3.1 suppresses the lineage potential of skeletal muscle. *Nucleic Acids Res.* **43**, 775–786 (2015).
65. G. Dennis Jr., B. T. Sherman, D. A. Hosack, J. Yang, W. Gao, H. C. Lane, R. A. Lempicki, DAVID: Database for annotation, visualization, and integrated discovery. *Genome Biol.* **4**, P3 (2003).
66. D. Kurotaki, N. Osato, A. Nishiyama, M. Yamamoto, T. Ban, H. Sato, J. Nakabayashi, M. Umehara, N. Miyake, N. Matsumoto, M. Nakazawa, K. Ozato, T. Tamura, Essential role of the IRF8-KLF4 transcription factor cascade in murine monocyte differentiation. *Blood* **121**, 1839–1849 (2013).

Acknowledgments

Funding: This work was supported by a Grant-in-Aid for Young Scientist (A/B); JSPS Fellows (14 J01375); Scientific Research on Innovative Areas (Comprehensive Brain Science Network and Foundation of Synapse and Neurocircuit Pathology); Challenging Exploratory Research from the Ministry of Education, Science, Sports, and Culture of Japan; and research foundations from the general insurance association of Japan. **Author contributions:** K.Ko. designed and performed most of the experiments with technical help from S.Y., T.Tama., K.Y.,

K.Ku., K.O., T.M., M.T., T.Tamu., Y.M., K.H., and K.I., analyzed the data, and wrote the manuscript. Y.O. performed RNA-seq analysis. M.H. and K.KI. analyzed the data of LMD. T.S. generated and analyzed bone marrow chimeric mice. V.R.E., Y.I., and Y.N. designed the studies and supervised the overall project. S.O. designed the studies, supervised the overall project, and performed the final manuscript preparation. **Competing interests:** The authors declare that they have no competing interests. **Data and materials availability:** All data needed to evaluate the conclusions in the paper are present in the paper and/or the Supplementary Materials. Additional data related to this paper may be requested from the authors. All RNA-seq data are available at the DDBJ under accession code DRA003810.

Submitted 29 September 2018
Accepted 11 April 2019
Published 15 May 2019
10.1126/sciadv.aav5086

Citation: K. Kobayakawa, Y. Ohkawa, S. Yoshizaki, T. Tamaru, T. Saito, K. Kijima, K. Yokota, M. Hara, K. Kubota, Y. Matsumoto, K. Harimaya, K. Ozato, T. Masuda, M. Tsuda, T. Tamura, K. Inoue, V. R. Edgerton, Y. Iwamoto, Y. Nakashima, S. Okada, Macrophage centripetal migration drives spontaneous healing process after spinal cord injury. *Sci. Adv.* **5**, eaav5086 (2019).